

Cite this: DOI: 00.0000/xxxxxxxxxx

Ensemble Effects of Explicit Solvation on Allylic Oxidation

Hung M. Le,^{*a} Mariano Guagliardo,^{b‡} Anne E. V. Gorden,^{b‡} and Aurora E. Clark^{*a,c}Received Date
Accepted Date

DOI: 00.0000/xxxxxxxxxx

Umbrella-sampling density functional theory molecular dynamics (DFT-MD) has been employed to study the full catalytic cycle of the allylic oxidation of cyclohexene using a Cu(II) 7-amino-6-((2-hydroxybenzylidene)amino)quinoxalin-2-ol complex in acetonitrile to create cyclohexenone and H₂O as products. In comparison to gas-phase DFT, the solvent effect is observed as the rate determining allylic H-atom abstraction step has a free energy barrier of 12.1 ± 0.2 kcal/mol in solution. During the cycle, the explicit solvation and ensemble sampling of solvent configurations reveals important dehydrogenation and re-hydrogenation steps of the -NH₂ group bound to the Cu-site that are essential to catalyst recovery. This work illustrates the importance of ensemble solvent configurational sampling to reveal the breadth of processes that underpin the full catalytic cycle.

1 Introduction

The oxidation of an allylic CH₂ group to a carbonyl is an important process in multi-step organic syntheses.^{1,2} Consider that α,β -unsaturated enones or 1,4-enediones have been utilized as essential building components in the synthesis of numerous natural compounds and drug precursors.^{3–7} In general, allylic oxidation can be efficiently activated using tert-butyl hydroperoxide (TBHP) with the addition of metal catalysts.^{8–13} Cu(II) complexes have been of particular interest as copper is relatively economical and environmentally benign. For example, Yao et al. synthesized a stable aryl-Cu(III) complex that was employed for C-H activation, resulting in very good yields under aerobic conditions.¹⁴ Wang and coworkers have synthesized a Cu(II) complex for dehydrogenative aminooxygenations, wherein the Cu oxidation state was demonstrated to convert from (Cu(II) to Cu(III)).¹⁵ By allowing a Cu(II)-superoxide complex to react with acyl chloride substrates, Pirovano and co-workers found the resultant complex to be a reactive nucleophile, which could be subsequently be employed for Baeyer–Villiger oxidations of aldehydes.¹⁶ More recently, C-H bond activation of methylene groups has been achieved using a triazole based ligand and mCPBA,¹⁷ and a bioinspired Cu(II) complex was used in the hydroxylation of benzene under mild conditions.¹⁸ With the aim of developing

new, economically advantageous catalysts possessing increased sustainability for allylic oxidations, Wu and co-workers¹⁹ developed a Cu(II) 2-quinoxalinol salen complex which affected the oxidation of allylic species without the common additional requirements of high heat or long reaction times. In a subsequent study, such a catalyst was applied with TBHP acting as an oxidant, and the oxidation of a variety of olefin substrates was reported with high yields.²⁰ The use of Cu(II) catalysts in the functionalization of organic structures both with and without the addition of peroxides has also recently been reviewed.²¹ A detailed analysis of such catalytic mechanisms can provide an improved understanding of their nature, and subsequently lead to the strategic design of new improved catalysts.

The catalyst of interest in this work is Cu(II) 7-amino-6-((2-hydroxybenzylidene)amino)quinoxalin-2-ol, first reported in 2014.²² This catalyst was developed to limit interference from free radical reactions; at the same time, it was found to demonstrate excellent efficiency in allylic oxidation reactions. However, prior gas-phase density functional theory study of the reaction mechanism resulted in a relatively high estimation of reaction barriers; the rate-determining step of H-atom abstraction was reported to consume 43.7 kcal/mol, while the step to release cyclohexenone required 37.5 kcal/mol. Further, the final steps to retrieve the initial catalytic structure was not described.

In recent years, DFT-based molecular dynamics^{23–25} have achieved sufficient computational efficiency to support broader application in the study of catalytic cycles that account for the ensemble and dynamic evolution of solvent and solutes. This method is a significant improvement over more widespread embedding methods that attempt to include solvent effects by placing the solute of interest within a dielectric continuum. In the latter, direct solute-solvent interactions are not considered, which

^a Department of Chemistry, Washington State University, Pullman, Washington 99164, United States

^b Department of Chemistry and Biochemistry, Texas Tech University, Lubbock, Texas 79430, United States

^c Pacific Northwest National Laboratory, Richland, Washington 99352, United States
Email: hung.le2@wsu.edu, auclark@wsu.edu

† Electronic Supplementary Information (ESI) available: . See DOI: 00.0000/00000000.

hampers the study of catalytic processes where the solvent may play a more prominent role. Further, the ensemble sampling of solute and solvent configurations can reveal important mechanistic features that are not observed when taking a more prescribed approach that involves a pre-defined reaction coordinate with limited degrees of freedom.

The current work demonstrates a new reaction scheme for the allylic oxidation of cyclohexene in acetonitrile that has significantly lowered free energies for reaction relative to prior gas-phase DFT studies, and it further samples the multiple reaction pathways. Over the course of the reaction, supporting evidence is provided for the previously reported electronic structure changes reported by Storr *et al.*²⁶ of square planar Cu(II) that undergoes reversible oxidation to Cu(III) during the course of the C-H bond activation. The recovery of methyl peroxide (CH₃OO-) attached to the Cu is obtained to close the catalytic cycle. The new reaction scheme involves the bound -NH₂ of the ligand acting as an H-atom reservoir, that - when combined with the ensemble solvation - yields free energy barriers for the entire catalytic cycle in good agreement with experimental observations.

2 Computational Details

2.0.0.1 MD Simulation Protocol. The Cu(II) 7-amino-6-((2-hydroxybenzylidene)amino)quinoxalin-2-ol complex (**1**) is a slightly simplified catalyst model with respect to the experimental system,²² wherein the two t-butyl groups (-C(CH₃)₃) on the quinoxalin-2-ol and salicylidene residues are replaced by -H because they are far from the reactive site that consists of Cu(II) and the attached methyl peroxide (-OOCH₃). The molecular structure of catalyst **1** is shown in Figure 1 along with the subsequent reaction intermediates (*vide infra*).

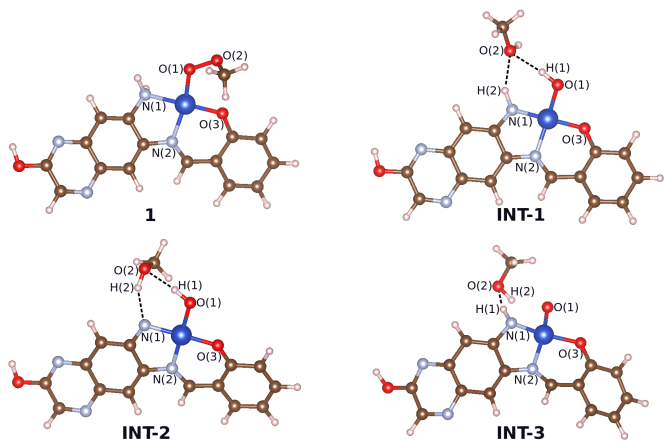


Fig. 1 Molecular structure of catalyst **1** Cu(II) 7-amino-6-((2-hydroxybenzylidene)amino)quinoxalin-2-ol, and the three subsequent intermediates **INT1**, **INT2**, **INT3**. Color codes for atomic representation: Cu (deep blue), C (brown), O (red), N (light blue), hydrogen (white).

The isolated structure **1** and reactants (cyclohexene and molecular oxygen) as well as the solvating molecules (i.e. acetonitrile as solvent) are initially optimized using the B3LYP functional^{27–29} and 6-31G(d) basis set^{30,31} in the Gaussian 16 package.³² Then, the catalyst, reactants, and 60 acetonitrile (357 atoms in total)

are initialized by random insertion into a periodic cubic box using the Packmol code.³³ The size of the periodic box with edge-length of 17.52 Å is obtained as a result of system equilibration using the NPT-ensemble with the stochastic velocity rescaling method³⁴ within DFT-MD for 2 ps at 350 K (the experimental temperature²²), in the Quantum Espresso package.³⁵ The PBE functional^{36–38} was employed with the DFT-D3, long-range London dispersion interaction classical interaction scheme proposed by Grimme,³⁹ to provide empirical correction terms to the long-range interactions. The Rappe-Rabe-Kaxiras-Joannopoulos ultrasoft (RRKJUS) plane-wave basis set and pseudo-potential^{40–42} was employed for all participant atoms. To compromise with computational expense for such a large system, we use Γ -point calculations. A standard time step of 20 atomic Rydberg time-units (~ 0.968 fs) is used at every MD step, and the Verlet integration method⁴³ is employed to integrate the classical equations of motion. The density of the NPT equilibrated system is 0.77 g/cm³. The slightly low density relative to experimental bulk acetonitrile (density = 0.79 g/cm³) is anticipated based upon the small simulation box size wherein about 20% of the volume is occupied by the solutes.

2.0.0.2 Umbrella Sampling of the Catalytic Cycle. The umbrella sampling technique^{44–46} enhances sampling along a specific reaction channel and employed the NVT ensemble at the experimental temperature of 350 K,²² using the velocity rescaling thermostat.⁴⁷ In each bin, we apply a harmonic-bias potential to put a constraint on the chosen reaction coordinate. The reaction coordinate varies for each step in the catalytic cycle and is described in the Results and Discussion. Each harmonic potential adopts the form:

$$V(\chi) = \frac{1}{2} \kappa (\chi - \chi_e)^2, \quad (1)$$

where κ is the spring constant (kcal/Å²), and χ_e is the location for constraining the reaction coordinate (Å). To obtain good statistical data in umbrella sampling, the bin size is 0.1 Å, and 200 DFT-MD steps are sampled in each bin. To verify that the use of 200 DFT-MD steps is sufficient for the convergence of free energy approximation, we carry out several tests with various number of DFT-MD steps (150-200) for each reaction step as shown by Figures S1-S6 in the Supporting Information. The overlap of umbrella-sampling bins are presented in Figures S7-S12.

From the biased MD data obtained at each step, the average distribution function can be computed statistically through a Boltzmann-weighted scheme:

$$\langle \rho(\chi_e) \rangle = \frac{\int \delta(\chi_e - \chi) e^{-V(q)/k_B T} dq}{\int e^{-V(q)/k_B T} dq}, \quad (2)$$

In the above equation, k_B is the Boltzmann constant, and T is the chosen temperature (350 K) for simulation. Then, the potential of mean force (PMF) demonstrating the free-energy profile for a reaction along the user-defined internal coordinate χ can be calculated:⁴⁸

$$\omega(\chi) = -k_B T \ln(\langle \rho(\chi) \rangle), \quad (3)$$

For the investigated reaction channels in this study, the PMF approximations which follow equations 2 and 3 are executed us-

ing the weighted-histogram analysis method (WHAM) as implemented by Grossfield.^{49,50}

3 Results and Discussion

3.1 Formation of cyclohexenone

The first investigation was to probe the H-atom abstraction as activated by the peroxy ligand attached to Cu(II), which is the rate-determining step toward product formation and forms cyclohexene radical. Within the umbrella sampling, two different abstraction steps are considered, where the reaction coordinate consists of either the allylic H-site being approached by O(1) or O(2) of the catalyst (atom labels denoted in Figure 1) and establishing a new O-H bond, thus breaking the O-O peroxide bond. The cyclohexene hydrogen is initially placed 4.8 Å from O(1) or O(2) of the catalyst, and using a window size of 0.1 Å the distance is systematically decreased. In the initial stage having $r_{O(1)-H}$ or $r_{O(2)-H} (\geq 2.7 \text{ \AA})$, a force constant for the harmonic bias of ($\kappa = 50 \text{ kcal/mol\AA}^2$) is employed, which is increased to $100 \text{ kcal/mol\AA}^2$, and at the transition state of new O-H bond formation (around 1.2 Å), a high force constant of $400 \text{ kcal/mol\AA}^2$ is used. It is practical to perform manual tuning of the harmonic constant during umbrella sampling to enforce good overlap between distance bins.⁵¹ The long-range interactions at large distances are weak and require only a small κ , whereas the formation of a hydroxide (O-H) covalent bond at short distances necessitates a large κ . As shown in Figure 2(a), the PMF curve of the O(1)...H channel of **1** shows a free energy barrier of $12.1 \pm 0.2 \text{ kcal/mol}$, which is more favorable than the O(2)...H channel at $15.6 \pm 0.4 \text{ kcal/mol}$. The favorability of the O(1)...H reaction channel is in good agreement with the theoretical mechanism proposed in previous work;²² however, those gas-phase calculations predicted an unreasonable potential energy barrier of 43.7 kcal/mol.

The next step was to follow the rest of the catalytic cycle for both reaction channels based upon the hydrogen atom abstraction by either O(1) or O(2). Following the first reaction channel of O(1) abstraction, a hydroxyl (-OH) residue is established at the O(1) site, which bonds directly to the Cu(II), while $\text{CH}_3\text{O}(2)\cdot$ is formed along with the resultant cyclohexene radical. Interestingly, the neighboring -N(1)H₂ group plays a role as the hydrogen atom source to stabilize the radical site, wherein $\text{CH}_3\text{O}(2)\cdot$ quickly abstracts the hydrogen atom from the N(1)H₂ to produce methanol. This is a fast and spontaneous process that occurs within 0.2 ps after the O(1)-O(2) dissociation. In the second reaction channel, based upon the O(2) allylic H-atom abstraction, an alcohol residue is established at O(2). Methanol is produced directly as a product of this reaction step, while the resulting O(1) radical quickly abstracts a hydrogen atom from the nearby -N(1)H₂ to become -O(1)-H bound to the Cu. Thus, somewhat surprisingly, both of the reaction channels from O(1) and O(2) abstractions lead to the formation of methanol and Cu-O-H, and the dehydrogenation of the coordinated -N(1)H₂ to -N(1)H (see Scheme 1). The intermediate Cu-complex is labeled as **INT1** obtained from catalyst **1**, as illustrated in Figure 1. The unique dehydrogenation behavior is revealed by the ensemble sampling of different degrees of freedom of the solutes and solvent and would

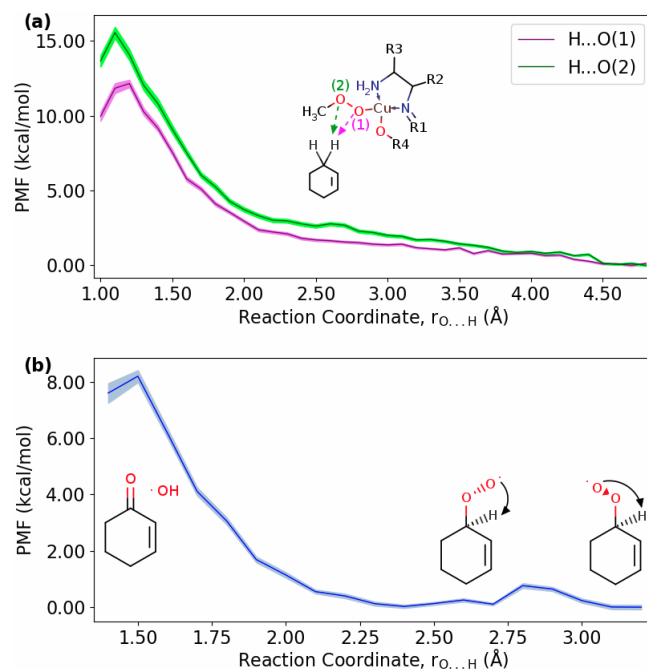
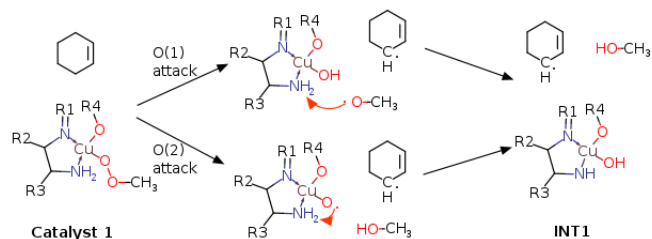


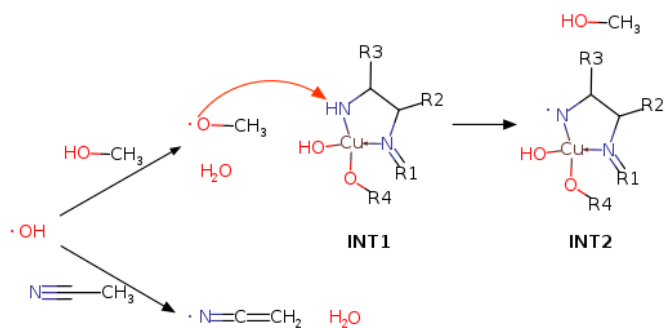
Fig. 2 (a) PMF (Eqn. 3) for O(1)...H and O(2)...H abstraction channels by catalyst **1**, (b) PMF for the formation of cyclohexenone and ·OH radical.



Scheme 1 Two reaction branches of **1** associated with the O(1) or O(2) abstraction of the allylic cyclohexene hydrogen atom lead to the formation of cyclohexene radical and methanol, and the intermediate structure **INT1**.

not be anticipated from a gas-phase study.

The second step of the reaction does not involve **INT1**, and instead consists of the cyclohexene radical being oxidized by molecular oxygen to form cyclohexenone. The system containing **INT1**, molecular oxygen and the cyclohexene radical was equilibrated for 1.5 ps at 350 K, wherein the O₂ diffused to the cyclohexene radical and reacted to form the cyclohexene-peroxy radical. This species adopts a *trans* conformation about the O-O-C-H and as such, the equilibrium distance between the terminal oxygen atom and allylic hydrogen atom is 3.2 Å. A rotational barrier must exist along this dihedral, as rotation does not readily occur. Thus, this species is somewhat long-lived and prevents the observation of further reaction within the 1.5 ps of equilibrated trajectory. Umbrella sampling was then performed that brought the terminal O-atom to the allylic hydrogen atom (Figure 2(b)). This first consists of O-O bond rotation around the O-C axis in order to approach the targeted hydrogen site, which has a barrier of ca. 0.8 kcal/mol within the PMF (see Figure 2(b)). As the hydroxyl O...H



Scheme 2 Activity of $\cdot\text{OH}$ radical in the solution.

bond distance is systematically reduced in the PMF, a free energy barrier of 8.2 ± 0.2 kcal/mol is observed at a hydroxyl O...H bond distance is around 1.5 \AA that corresponds to the hydroxyl O-H bond formation and cleavage of the peroxy O-O bond. In the last umbrella sampling step at 1.4 \AA , the barrier is overcome, wherein the newly formed hydroxide radical ($\cdot\text{OH}$) departs and cyclohexanone is created. The hydroxide radical ($\cdot\text{OH}$) is highly reactive and will abstract hydrogen atoms from nearby molecules, including the methanol produced from the first step of the catalytic cycle or other available solvent molecules (Scheme 2). Both processes occur very rapidly and without a barrier in equilibrium trajectories after the formation of the hydroxide radical ($\cdot\text{OH}$). In the reaction with methanol, a hydroxymethyl radical ($\text{CH}_3\text{O}\cdot$) is produced which is observed to spontaneously abstract the final hydrogen atom from N(1) in INT1 to form the second intermediate of the catalytic cycle INT2 in Figure 1 and Scheme 2. In the instance where the hydroxide radical ($\cdot\text{OH}$) abstracts a hydrogen atom from acetonitrile, the resulting radical $\text{H}_2\text{CCN}\cdot$ is formed, which has the ability to re-enter the hydrogen abstraction cycle; however, this reaction pathway was not pursued for further analysis. Examining the process of system equilibration before the final product formation (1 ps), we observe that O(2) in intermediate INT1 retains a long-range hydrogen bond with H(2) as shown in the radial distribution function (RDF) plots in Figure S15. The O(2)-H(1) hydrogen bond facilitates (or preorganizes) O(2) being able to abstract H(2) from N(1) to yield the intermediate INT2.

The evolution of **1** to intermediates INT1 and then INT2 involves significant changes to the electronic structure. Prior experimental study of related complexes using UV-vis spectroscopy, magnetic susceptibility, and X-ray crystallography, have indicated the switch of the Cu oxidation state (from Cu(II) to Cu(III)) and a dynamic equilibrium between spin states in a square-planar organometallic complex during the catalytic cycle.²⁶ To examine the change in electronic structure during the formation of the cyclohexenone, Natural Population Analysis (NPA)⁵² was performed to identify atomic partial charges, and the atomic spin density was analyzed. Both single point and gas-phase geometry optimized clusters consisting of the catalyst and two acetonitrile molecules that are closest to the reactive site were examined. The single point calculations employed the B3LYP/aug-cc-pVDZ⁵³ functional/basis-set combination, while the geometry

Table 1 NPA charges (q) and spin density (ρ) of Cu and its coordinated atoms in catalyst **1** and intermediates INT1 and INT2 obtained from single point B3LYP/cc-pVDZ calculations sampled from the DFT-MD trajectory.

Site	1		INT1		INT2	
	q	ρ	q	ρ	q	ρ
Cu	0.99	0.56	0.99	0.00	0.96	0.06
N(1)	-0.91	0.09	-0.74	0.00	-0.50	0.70
O(1)	-0.57	0.16	-0.94	0.00	-0.85	0.01
N(2)	-0.59	0.07	-0.50	0.00	-0.55	0.02
O(3)	-0.74	0.09	-0.68	0.00	-0.61	0.03

Table 2 The Cu-ligand bond distances (\AA) in catalyst **1** and intermediates INT1 and INT2 obtained from B3LYP/6-31g(d) optimizations.

Bond	1	INT1	INT2
Cu-N(1)	2.04	1.83	1.85
Cu-O(1)	1.85	1.79	1.78
Cu-N(2)	1.96	1.91	1.89
Cu-O(3)	1.90	1.86	1.87

optimization was performed with the smaller 6-31g(d) basis,^{30,31} followed by NPA using this basis set. Herein, the focus is the single-point calculations, while the smaller basis set calculations are presented in the Supplementary Information. As observed in Table 1, the charge of Cu during the catalytic cycle is relatively unchanged (q_{Cu} ca. 1.0); however, the unpaired electron density is changed from ca. 0.5 in **1** to essentially zero in INT1 and INT2. Concomitantly, there is charge migration from N(1) and O(3) (which become more positively charged) to O(1) (which becomes more negatively charged), while there is growth of unpaired electron density on N(1), during the formation of INT2. In terms of bond distances given by B3LYP/6-31g(d) structural optimizations, the Cu-N(1) and Cu-O(1) bonds in **1** are 2.04 \AA and 1.85 \AA , respectively (Table 2). In intermediate INT1, the Cu-N(1) distance drops significantly to 1.83 \AA ($> 10\%$). The Cu-O(1) bond is somewhat shortened to 1.79 \AA . In intermediate INT2, the Cu-N(1) and Cu-O(1) bonds are 1.85 \AA and 1.78 \AA , which are nearly the same as in INT1. The drop in bond distance herein is in good agreement with the experimental and theoretical observations in the previous report of Storr *et al.*²⁶, which clearly pointed out the slight decrease of ionic radius of square-planar Cu upon the oxidation from II to III. In that report, the square-planar Cu site was surrounded by two nearly-equivalent O and two nearly-equivalent N ligands. In the Cu(II) state, the experimental (and calculated) Cu-O and Cu-N bonds are 1.89 (1.90) \AA and 1.91 (1.93) \AA , respectively; while in the Cu(III) state, the experimental (and calculated) Cu-O and Cu-N bonds are 1.84 (1.84) \AA and 1.88 (1.87) \AA .²⁶ Interestingly enough, it is observed in this case study that the Cu-N(1) bond length decreases by a greater extent when undergoing transformation from **1** to INT1.

3.2 Recovery of the initial catalyst

At this stage in the catalytic cycle, cyclohexenone has been obtained and two side products have been created (H_2O and CH_3OH) alongside the intermediate INT2 (Figure 1). Impor-

tantly, within the equilibrated system of **INT2**, methanol forms a stable hydrogen bond with N(1) through the N(1)-H(2) and O(2)-H(1) hydrogen bonds, as shown in the RDF plot in Figure S16. Based upon the spontaneous H-atom abstraction by the methoxy radical from -N(1)H(2) that created **INT2**, it is considered unlikely that the reverse reaction will contribute to catalyst recovery. As such, to consider how N(1) may recover its H-atoms and the O(1)-O(2) peroxy bond may reform, we first examine the H-atom abstraction from O(1) by the N(1) site.

The intermediate **INT2** shown is first equilibrated in acetonitrile prior to executing the umbrella sampling along the N(1)...H(1) distance. The process of H-atom transfer starts to occur at 1.7 Å and the N(1)-H(1) distance is at a minimum at 1.16 Å. A free energy barrier of 11.0 ± 0.2 kcal/mol is observed for this process, which creates an O(1) radical (Figure 3(a)). After the last umbrella sampling step, we allow the system to equilibrate, and H(1) maintains its covalent bond with N(1), establishing the intermediate **INT3**. This intermediate structure forms a long-lived hydrogen bond with methanol (CH₃O(2)H(2)) via the long-range O(2)-H(1) linkage, as illustrated by the RDF data in Figure S17.

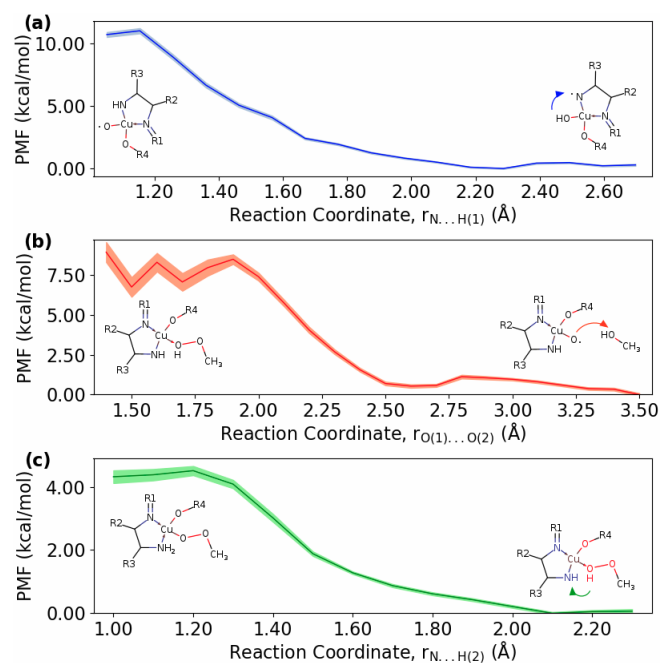


Fig. 3 (a) PMF (Eqn. 3) of the N(1)-H(1) bond formation leading to the establishment of O(1) radical site, to form intermediate **INT3**, (b) PMF of the O(1)-O(2) bond formation to re-establish peroxide, (c) PMF of the N(1)-H(2) bond formation to recover the initial catalyst.

The above simulation of N(1)-H(1) recombination allows us to formulate a new perspective about driving forces that may allow the O(1) and O(2) sites in **INT2** to reform their peroxy bond via the ability of N(1) to abstract an H-atom from O(1), thus creating a reactive O-site. The next step to recover the initial catalyst is thus explored by sampling the O(1)...O(2) distance coordinate from the equilibrated **INT3**, which sets the O(1)-O(2) distance in the system to be around 3.5 Å. During the system equilibration, the RDF for the O(2)-H(1) pair (Figure S17) indicates a hydrogen

bond between O(2) and H(1) at around 2 Å. As O(1) approaches closer to O(2) at the local minimum when the O(1)-O(2) distance is 2.7 Å, H(2) quickly migrates toward O(1) and makes a strong covalent bond. After 19 umbrella sampling steps (step size = 0.1 Å), the system seems to be trapped in another local minimum where the peroxide O-O distance is around 1.7 Å, as shown in Figure 3(b). Interestingly, when the system is equilibrated for 0.5 ps at the current O(1)-O(2) distance of 1.7 Å, it would favor to release ·CH₃O(2) radical, which can re-enter another catalytic cycle, while the -O(1)-H(2) residue remains bonding with Cu. Later, the actual minimum for the O(1)-O(2) peroxide bond formation is located around 1.5 Å. The free energy barrier of this process is determined as 8.5 ± 0.6 kcal/mol, which is found around the O(1)-O(2) distance of 1.9 Å. Continuing to sample toward the O(1)-O(2) equilibrium distance around 1.4-1.5 Å, we find that the methyl peroxide (CH₃OOH) that is formed maintains the O(1)-Cu bond.

The final umbrella sampling process is carried out with the recovery of the catalyst, in which we investigate the return of H(2) to N(1). After the O(1)-O(2) peroxide bond is established, the whole system is equilibrated for 1 ps at 350 K. The equilibrated N(1)-H(2) distance after this process is just 2.3 Å. During the umbrella sampling (Figure 3(c)), the free barrier is 4.5 ± 0.1 kcal/mol at the N(1)-H(2) of ca. 1.3 Å. After overcoming the harmonic sampling step around 1.2 Å, the original structure of catalyst is finally recovered.

The overall reaction mechanism observed by umbrella sampling MD in this study is presented in Scheme 3. It should be noted that we only present the primary reaction channels with the most favorable free energies barriers in the scheme. Overall, a water molecule is obtained as a side product besides the targeted product, cyclohexenone. According to this cycle, at the completion of reaction, the catalyst can be fully recovered, which is revealed by our umbrella sampling MD data. Although methanol is formed as an intermediate product within this cycle, it is consumed when the original catalyst is restored.

- and T. D. P. Stack, *Journal of the American Chemical Society*, 2008, **130**, 15448–15459.
- 27 A. D. Becke, *The Journal of Chemical Physics*, 1993, **98**, 5648–5652.
 - 28 C. Lee, W. Yang and R. G. Parr, *Phys. Rev. B*, 1988, **37**, 785–789.
 - 29 P. J. Stephens, F. J. Devlin, C. F. Chabalowski and M. J. Frisch, *The Journal of Physical Chemistry*, 1994, **98**, 11623–11627.
 - 30 G. A. Petersson, A. Bennett, T. G. Tensfeldt, M. A. Al-Laham, W. A. Shirley and J. Mantzaris, *The Journal of Chemical Physics*, 1988, **89**, 2193–2218.
 - 31 G. A. Petersson and M. A. Al-Laham, *The Journal of Chemical Physics*, 1991, **94**, 6081–6090.
 - 32 M. J. Frisch, G. W. Trucks, H. B. Schlegel, G. E. Scuseria, M. A. Robb, J. R. Cheeseman, G. Scalmani, V. Barone, G. A. Petersson, H. Nakatsuji, X. Li, M. Caricato, A. V. Marenich, J. Bloino, B. G. Janesko, R. Gomperts, B. Mennucci, H. P. Hratchian, J. V. Ortiz, A. F. Izmaylov, J. L. Sonnenberg, D. Williams-Young, F. Ding, F. Lipparini, F. Egidi, J. Goings, B. Peng, A. Petrone, T. Henderson, D. Ranasinghe, V. G. Zakrzewski, J. Gao, N. Rega, G. Zheng, W. Liang, M. Hada, M. Ehara, K. Toyota, R. Fukuda, J. Hasegawa, M. Ishida, T. Nakajima, Y. Honda, O. Kitao, H. Nakai, T. Vreven, K. Throssell, J. A. Montgomery, Jr., J. E. Peralta, F. Ogliaro, M. J. Bearpark, J. J. Heyd, E. N. Brothers, K. N. Kudin, V. N. Staroverov, T. A. Keith, R. Kobayashi, J. Normand, K. Raghavachari, A. P. Rendell, J. C. Burant, S. S. Iyengar, J. Tomasi, M. Cossi, J. M. Millam, M. Klene, C. Adamo, R. Cammi, J. W. Ochterski, R. L. Martin, K. Morokuma, O. Farkas, J. B. Foresman and D. J. Fox, *Gaussian~16 Revision C.01*, 2016, Gaussian Inc. Wallingford CT.
 - 33 L. Martínez, R. Andrade, E. G. Birgin and J. M. Martínez, *Journal of Computational Chemistry*, 2009, **30**, 2157–2164.
 - 34 G. Bussi, T. Zykova-Timan and M. Parrinello, *The Journal of Chemical Physics*, 2009, **130**, 074101.
 - 35 P. Giannozzi, O. Andreussi, T. Brumme, O. Bunau, M. B. Nardelli, M. Calandra, R. Car, C. Cavazzoni, D. Ceresoli, M. Cococcioni, N. Colonna, I. Carnimeo, A. D. Corso, S. de Gironcoli, P. Delugas, R. A. D. Jr, A. Ferretti, A. Floris, G. Fratesi, G. Fugallo, R. Gebauer, U. Gerstmann, F. Giustino, T. Gorni, J. Jia, M. Kawamura, H.-Y. Ko, A. Kokalj, E. Küçükbenli, M. Lazzeri, M. Marsili, N. Marzari, F. Mauri, N. L. Nguyen, H.-V. Nguyen, A. O. de-la Roza, L. Paulatto, S. Poncé, D. Rocca, R. Sabatini, B. Santra, M. Schlipf, A. P. Seitsonen, A. Smogunov, I. Timrov, T. Thonhauser, P. Umari, N. Vast, X. Wu and S. Baroni, *Journal of Physics: Condensed Matter*, 2017, **29**, 465901.
 - 36 J. P. Perdew, K. Burke and M. Ernzerhof, *Phys. Rev. Lett.*, 1996, **77**, 3865–3868.
 - 37 J. P. Perdew, K. Burke and M. Ernzerhof, *Phys. Rev. Lett.*, 1997, **78**, 1396–1396.
 - 38 Y. Zhang and W. Yang, *Phys. Rev. Lett.*, 1998, **80**, 890–890.
 - 39 S. Grimme, J. Antony, S. Ehrlich and H. Krieg, *The Journal of Chemical Physics*, 2010, **132**, 154104.
 - 40 D. Vanderbilt, *Phys. Rev. B*, 1990, **41**, 7892–7895.
 - 41 A. M. Rappe, K. M. Rabe, E. Kaxiras and J. D. Joannopoulos, *Phys. Rev. B*, 1990, **41**, 1227–1230.
 - 42 A. Dal Corso, *Computational Materials Science*, 2014, **95**, 337–350.
 - 43 L. Verlet, *Phys. Rev.*, 1967, **159**, 98–103.
 - 44 G. Torrie and J. Valleau, *Journal of Computational Physics*, 1977, **23**, 187–199.
 - 45 J. Kästner, *Computational Molecular Science*, 2011, **1**, 932–942.
 - 46 W. You, Z. Tang and C.-e. A. Chang, *Journal of Chemical Theory and Computation*, 2019, **15**, 2433–2443.
 - 47 E. Braun, S. M. Moosavi and B. Smit, *Journal of Chemical Theory and Computation*, 2018, **14**, 5262–5272.
 - 48 B. Roux, *Computer Physics Communications*, 1995, **91**, 275–282.
 - 49 S. Kumar, J. M. Rosenberg, D. Bouzida, R. H. Swendsen and P. A. Kollman, *Journal of Computational Chemistry*, 1992, **13**, 1011–1021.
 - 50 A. Grossfield, *WHAM: an implementation of the weighted histogram analysis method, version 2.0.9*, <http://membrane.urmc.rochester.edu/content/wham/>.
 - 51 Q. Liao, *Computational Approaches for Understanding Dynamical Systems: Protein Folding and Assembly*, Academic Press, 2020, vol. 170, pp. 177–213.
 - 52 F. Martin and H. Zipse, *Journal of Computational Chemistry*, 2005, **26**, 97–105.
 - 53 D. E. Woon and T. H. Dunning, *The Journal of Chemical Physics*, 1993, **98**, 1358–1371.